Chapter 6
Two-Dimensional (2D) Damage Percolation/ Finite Element Modeling of Sheet Metal Forming

Experimental evidence and numerical simulation have established that ductile damage critically limits the formability of sheet metals (Gelin 1998; Hu et al. 2000; Tang et al. 1999). To accurately predict formability and to optimize material processing to achieve enhanced formability, it is important to understand how heterogeneously distributed micro-defects affect the macromechanical behaviour of sheet metal. Therefore, it is of both theoretical and practical interest to investigate damage evolution during sheet metal forming.

This research seeks to address the role of ductile damage in determining sheet metal formability. Of particular interest is the variable nature of material microstructures, for example the statistical variation in second phase particle size and spacing. It is well known that damage will first nucleate within closely spaced regions of second phase particles, known as particle clusters. It is considerably less well established how ductile damage then propagates outwards from particle clusters to establish macro-cracking and at what level damage becomes critical. Pilkey (1997) has conducted experimental research to examine the effect of particle clustering on ductile fracture of aluminum alloy sheets under various loading conditions. Detailed two-dimensional statistical data identifying various particle distribution properties has been acquired for Al-Si alloy sheets and then correlated with various formability trends (Pilkey 1997). The challenge exists, however, to properly include detailed statistical measures of microstructure in models of ductile fracture. Although there is an enormous collection of literature on the mechanical modelling of ductile fracture, none of the models available so far is able to properly include measured statistical particle fields.

Following the previous chapter, this chapter describes the extension of the percolation model to deal with ductile fracture in sheet metal forming. Strong strain gradients and heterogeneous second phase particle fields are the major concerns in this study. To achieve this goal, the damage percolation model is coupled with a Gurson (1977) based finite element (FE) model so that heterogeneity of microstructure and high strain gradients in sheet metal forming can be implemented using a coupled model.

Z. Chen and C. Butcher, *Micromechanics Modelling of Ductile Fracture*,
Solid Mechanics and Its Applications 195, DOI 10.1007/978-94-007-6098-1_6,

6.1 Stretch Flange Experiment

Automotive aluminum-magnesium alloys, AA5182 of 1.6 and 1.0 mm thicknesses, were employed in the present research. The nominal chemical compositions and the mechanical properties are listed in Tables 6.1 and 6.2. Stretch flange forming operations are commonly used in the automotive industry to fabricate inner door panels (Fig. 6.1). A blank with an inner cutout is clamped against a die while a punch moves downwards to form the flange through expansion of the cutout. A backup punch holds the sheet against the punch to make the bend at the punch profile radius. Drawbeads are often introduced to limit the rate of cutout expansion.

The repeated bending and unbending of the sheet, as it flows through the drawbeads can lead to damage initiation followed by necking at the cutout edge or tearing at the punch nose and around the profile radius. The amount of damage induced by the drawbeads in the sheet metal is of particular interest.

Table 6.1 Nominal chemical composition of AA5182, wt % (Finn MJ, private communication, 1999)

Si	Fe	Mg	Mn	Cu	Ti
0.08	0.3	4.6	0.33	0.04	

Table 6.2 Mechanical properties of AA5182 from uniaxial tensile tests (Finn MJ, private communication, 1999)

Gauge (mm)	σ_0 (MPa)	E (GPa)	ν
1.6	117.34	71.71	0.33
1.0	120.17	71.71	0.33

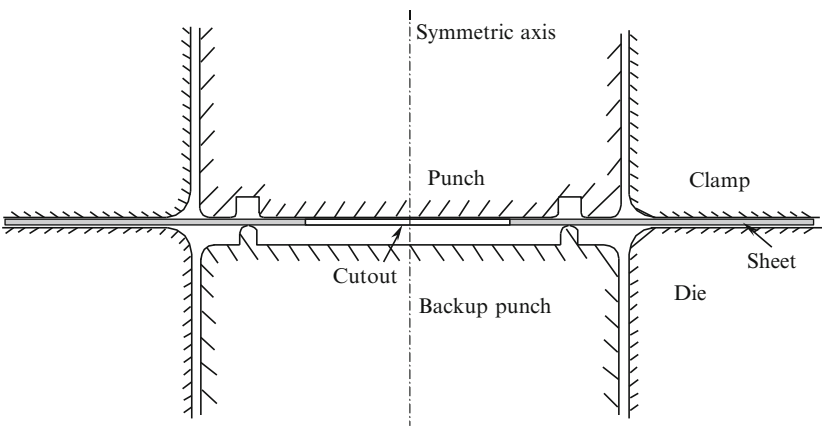

Fig. 6.1 Stretch flange forming tooling schematic

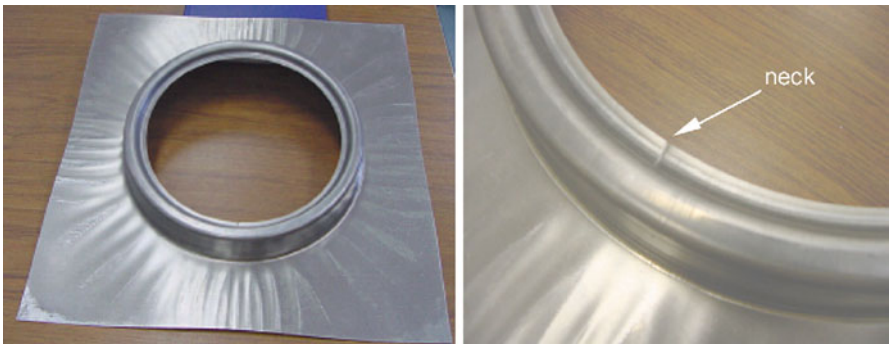

Fig. 6.2 A stretch flange sample fractured by inner edge necking (Reprinted with permission from Chen et al. (2005). Copyright: Elsevier)

A triple-action servo-hydraulic press, developed at the University of Waterloo (Cinotti 2003), was used in the stretch flange experiments. Figure 6.1 is a schematic of the z-flange tooling, which incorporates mating drawbeads on the main and backup punches. Drawbeads are used in commercial stretch flange operations to control or limit the rate of cutout expansion. Of interest in the current research is the level of damage induced by the bending-unbending of the sheet as it passes through the drawbeads. Detailed dimensions of the forming apparatus are given in Chen (2004). To capture the initiation of fracture during the stretch flange forming operation, a Piezotron® acoustic emission (AE) Sensor from Kistler Instrument Corp., was adapted to this tooling set by Orlov (private communication, 2003). The sensor is attached to the main punch to detect the acoustic pulse associated with the onset of cracking. The AE sensor is especially well suited for measuring AEs above 50 kHz.

Two different sets of experiments were conducted. The first is a crack detection test, where the punch motion is stopped immediately once the AE exceeds the threshold for crack initiation, as determined by relevant calibrating tests (Orlov O, private communication, 2003). Sheet specimens with cutout radii in the range of 88–98 mm, in increments of 2 mm, were tested to failure. The main purpose of this test is to investigate the effect of cutout size on the formability of stretch flanges. The second set of experiments comprised of a series of interrupted tests. For this part of the experiment, only the smallest (88 mm) and the largest (98 mm) cutout radii were considered. For each cutout size, the forming operation was interrupted at four different levels of punch depth, namely 25, 50, 75, and 90 % of the punch depth to fracture. The recovered samples were sectioned and their damage levels measured using metallographic, optical microscopy and image analysis methods. Damage development and strain path during the forming process is thereby captured within stretch flange samples.

A series of blanks were pressed in the first set of experiments in order to determine the limit punch depth that could be successfully formed without splitting as a function of the cutout radius. Two fracture modes were observed: one designated inner edge necking (Fig. 6.2) and the other as circumferential cracking

Fig. 6.3 A stretch flange sample fractured by circumferential cracking (Reprinted with permission from Chen et al. (2005). Copyright: Elsevier)

(Fig. 6.3). Fracture by inner edge necking can be arrested immediately after crack initiation (Fig. 6.2) using the AE sensor to stop the test. Crack arrest is possible due to the high strain gradient in the radial direction. Regions of lower strain in the outer area away from the cutout edge resist propagation of the neck and/or crack. However, fracture due to circumferential cracking at the punch nose propagates rapidly (Fig. 6.3) because of the axisymmetric nature of the crack orientation and high stresses in the sidewall. From the measured strain path of the interrupted stretch flanges, it is found that the radial necking-induced inner edge cracking is from the elevated circumferential uniaxial strains at the cutout, which is not thought to be damage-controlled. On the other hand, circumferential cracking at the punch nose is due to the biaxial stretching strain state which greatly promotes damage development and eventually causes ductile fracture. Details of strain path measurement can be found in Chen (2004). Here we focus on the damage-induced circumferential cracking at the punch nose.

The main punch displacement, backup punch force and clamping force were recorded by the load cells and displacement sensors mounted on the tooling and transferred to a PC for further analysis. Multi-channel servo-controllers were employed for signal conditioning and servo-control of the actuators. Further details of the apparatus and tooling are given by Cinotti (2003).

The percolation damage calculations presented in the previous chapter have served to demonstrate the nature of damage progression within a real second phase particle field; however, one limitation of these calculations is the assumption of a uniform strain field. In this chapter, modifications to the damage percolation approach are presented to allow consideration of non-uniform strain fields. The approach taken is to utilize a "loose coupling" of the percolation code with an elastic–plastic FE code that utilizes a Gurson-based damage model to describe the material constitutive response.

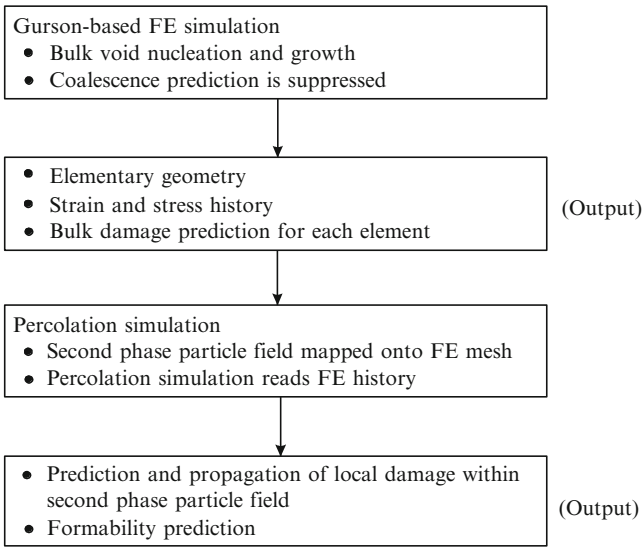

Fig. 6.4 A schematic of the one-way coupled FE-damage percolation model

The advantages to adopting such an approach are as follows:

- The FE code can readily handle the complex boundary conditions associated with metal forming operations, thus real strain gradients can be introduced into the percolation simulations;
- Bulk damage and constitutive softening predictions can be obtained using a Gurson-based constitutive model;
- The percolation code can utilize the FE stress, strain and bulk damage predictions and then predict the percolation of damage through the measured second phase particle field.

The approach in developing this "loose coupling" is to employ the FE model to handle the prediction of strain gradients and damage-induced softening, while the percolation calculations predict damage evolution within the tessellated second phase particle field, based upon deformation and bulk damage history from the FE calculation. Figure 6.4 outlines the nature of the coupling, which is essentially one-way with the FE history read in by the percolation code. Generally, the physical size of the simulation domain for the percolation code is much smaller; thus only a small region of the FE mesh, referred to as the mesh area of interest, or AOI, is considered in the percolation model.

The major changes required in the damage percolation model are to read in: (i) the initial mesh geometry for the AOI; and (ii) the nodal displacement history as well as element stress, strain and porosity histories. To accommodate the real deformation field, the measured second phase particle fields are mapped onto the mesh area of interest. Each particle is assigned a "parent element" and will experience the deformation and bulk damage history of the parent. The percolation code has been further

modified to support these coupled calculations in terms of the void nucleation, growth, coalescence and post-coalescence treatments, as outlined in Sects. 5.2, 5.3 and 5.4. Prior to discussing these modifications, the Gurson-Tvergaard-Needleman (GTN) constitutive model is presented, since it is adopted in the FE part of the coupled simulations.

6.2 GTN-Based Damage Model

The well-known Gurson-Tvergaard-Needleman (GTN) constitutive model (Gurson 1977; Tvergaard 1981; Tvergaard and Needleman 1984) is employed in the FE part of the coupled model. Since void coalescence and final failure are to be treated in the damage percolation part of the model, the usual void coalescence treatment in the GTN model has been suppressed. Thus, the GTN-based calculations are limited to predict the nucleation and growth of the bulk porosity (damage) and the damage-induced constitutive softening.

The GTN-damage model (Gurson 1977; Tvergaard 1981; Tvergaard and Needleman 1984) is based upon the pressure-sensitive yield function proposed by Gurson (1977):

$$\Phi = \left(\frac{\Sigma_{eq}}{\bar{\sigma}}\right)^2 + 2f^* q_1 \cosh\left(q_2 \frac{3\Sigma_m}{2\bar{\sigma}}\right) - 1 - q_1^2 f^{*2} = 0 \tag{6.1}$$

where f^* is the effective void volume fraction, Σ_{eq} and Σ_m are the von Mises effective stres s and hydrostatic stress, respectively, and $\overline{\sigma}$ is the matrix flow stress. The von Mises effective stress, Σ_{eq}, is defined by:

$$\Sigma_{eq} = \sqrt{\frac{3}{2}\Sigma'_{ij}\Sigma'_{ij}} \tag{6.2}$$

where Σ'_{ij} is the deviatoric stress component. The "q" coefficients are "calibration coefficients" introduced by Tvergaard (1981) to better represent void interaction effects in plastically deforming materials. The function f^* was introduced by Tvergaard and Needleman (1984) to account for the onset of void coalescence,

$$f^* = \begin{cases} f & \text{if } f \le f_c \\ f_c + \frac{f_u^* - f_c}{f_f - f_c}(f - f_c) & \text{if } f > f_c \end{cases} \tag{6.3}$$

in which, f_c is a critical porosity value at which void coalescence commences, f_f is the porosity value at failure and $f_u^* = 1/q_1$. It is seen from Eq. (5.3) that

fracture through void coalescence is assumed to initiate once the porosity reaches a critical value, f_c. In the current study, void coalescence is suppressed by specifying large values of f_c and f_f. Thus $f^* = f$ for all of the coupled simulations.

The rate of increase of void volume fraction is due to the growth of existing voids and the nucleation of new voids:

$$\dot{f} = \dot{f}_{growth} + \dot{f}_{nucleation} \tag{6.4}$$

Assuming the material is plastically incompressible, the growth of existing voids is related to the hydrostatic component of macroscopic plastic strain by:

$$\dot{f}_{growth} = 3(1-f)\dot{E}_{\text{hyd}} \tag{6.5}$$

The contribution of void nucleation will be material dependent. For the aluminum-magnesium alloys in this study, a plastic strain-controlled nucleation rule is adopted, that assumes that voids nucleate at second phase particles and there is a normal distribution of nucleation strain for the total population of particles (Chu and Needleman 1980),

$$\dot{f}_{nucleation} = A\dot{\bar{\varepsilon}}^p \tag{6.6}$$

in which

$$A = \frac{f_N}{S_N\sqrt{2\pi}} \exp\left[-\frac{1}{2}\left(\frac{\bar{\varepsilon}^p - \varepsilon_N}{S_N}\right)^2\right] \tag{6.7}$$

where $\bar{\varepsilon}^p$ is the effective plastic strain representing the microscopic strain-state in the matrix material. The term f_N represents the volume fraction of void-nucleating particles, while ε_N and S_N are the average and standard deviation of the strains at which particles nucleate voids. In the coupled calculations, values of ε_N and s_N were determined such that the void nucleation rate using Eqs. (6.6) and (6.7) closely matched those for the percolation model. Further elaboration of the nucleation model is given in Sect. 6.3.1.

The effective plastic strain in the matrix material is calculated according to the principle of work equivalence,

$$\dot{\bar{\varepsilon}}^p = \frac{\Sigma_{ij}\dot{E}^p_{ij}}{(1-f)\bar{\sigma}} \tag{6.8}$$

where $\dot{E}^p_{ij}$ is the rate of macroscopic plastic strain. The plastic flow in the material is taken from the uniaxial stress versus effective plastic strain curve obtained by uniaxial tensile tests.

6.3 Coupled Percolation Model – Damage Predictions

The percolation damage algorithm, as adapted to perform coupled predictions, largely follows that described in Chap. 4 of this thesis. Modifications are required, however, to handle the deformation and state information generated by the GTN-based damage predictions outlined in the previous section. The following sections describe the changes required in percolation model of Chap. 5 to accomplish this "one-way loose-coupling".

6.3.1 Void Nucleation

Void nucleation due to particle decohesion or cracking is directly related to the local plastic strain in the vicinity of a particle. Thus, in coupled model, it is assumed that once the equivalent plastic strain of its parent element attains the nucleation strain, i.e.

$$\bar{\varepsilon}^p \geq \varepsilon_n \tag{6.9}$$

the particle is nucleated and treated as a void, where ε_n is the nucleation strain of the specific particle.

At the current stage of implementation of the coupled calculations, the void nucleation treatment differs somewhat between the two parts of the model. The nucleation strains in the percolation code were treated in the same manner as was presented in Chap. 4; however, the predicted nucleation strain as a function of particle size was adjusted to better match recent results by Winkler (2003) for the aluminum-magnesium alloy AA5182. In that work, the nucleation parameters in Eqs. (5.6) and (5.7) were determined for 1.6 mm AA5754 and AA5182, to match measured bulk damage levels in the stretch flange samples (Chen 2004). The AA5182 samples exhibited high levels of damage and a nucleation strain of 0.2 was recommended by Winkler (2003). Note that a standard deviation (s_N) of 20 % was assumed for both alloys (Winkler 2003).

In the current research, detailed measured data concerning the particle nucleation strain as a function of particle size was not available, although such measurements are underway in related work (Winkler 2003). Instead, the form of the assumed relationship between nucleation strain was adjusted such that: (i) the average bulk nucleation strain matched the values determined by Winkler (2003); and (ii) the slope of the porosity evolution versus strain matched that predicted by the GTN model for the assumed values of s_N. Figure 6.5 shows the assumed dependence of nucleation strain as a function of particle size for both alloys. The bold curves were those matching the average nucleation strains determined by Winkler (2003). Recognizing that this description of nucleation strain is somewhat subjective and requires future validation, it was elected to consider two additional

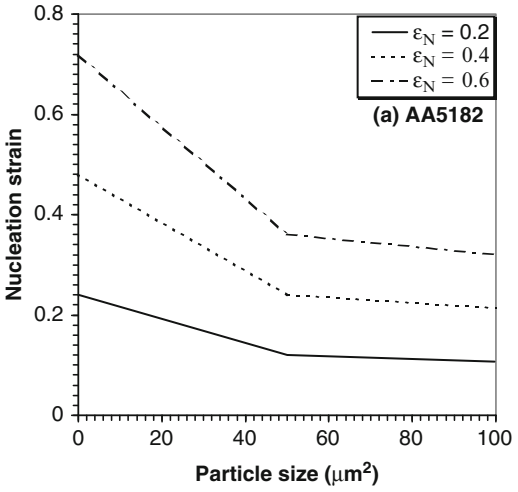

Fig. 6.5 Void nucleation strain versus particle size adopted in the percolation simulations corresponding to the nucleation strain (ε_N) used in the GTN-based FE calculation

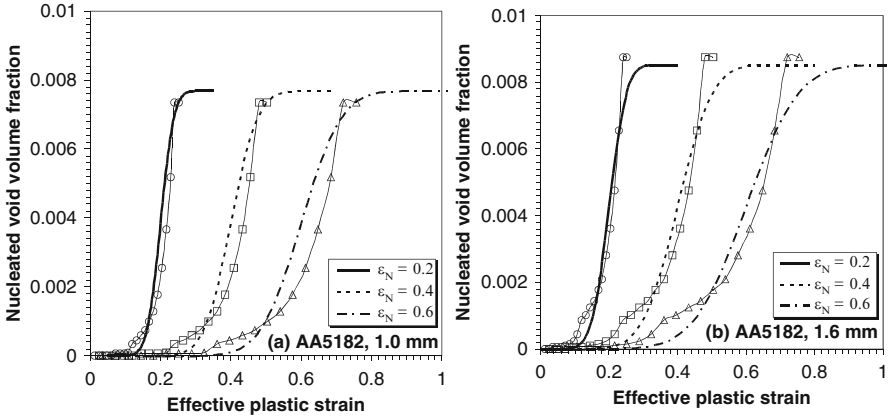

Fig. 6.6 Predictions of nucleated void volume fraction using the various void nucleation strains plotted in Fig. 5.2 (open symbols). Curves are predicted using corresponding values for ε_N and values for S_N in Table 5.1 (Reprinted with permission from Chen and Worswick (2008). Copyright: Elsevier)

levels of average nucleation strain to evaluate the effect of nucleation strain in a parametric fashion. Levels of $\varepsilon_N = 0.4$ and 0.6 were selected as being intermediate to the levels determined by Winkler. The nucleation curves using these levels are also plotted in Fig. 6.5 and were considered in the coupled percolation simulations.

By combining the functional dependence of particle nucleation strain on particle size in Fig. 6.5 with the measured particle size frequencies, it then becomes possible to predict the volume fraction of nucleated particles as a function of strain. This data is plotted for each alloy and thickness in Fig. 6.6 (open symbols).

Table 6.3 Controlling parameters in the GTN-based material model

f_N	**0.00768**	**0.00853**
f_0	0	0
ε_{N1}	0.2	0.2
ε_{N2}	0.4	0.4
ε_{N3}	0.6	0.6
s_N	15 %	15 %

In an effort to "synchronize" the Gurson nucleation prediction with the percolation model, values of s_N were determined for each sheet material to match the percolation predictions in Fig. 6.6 for each level of ε_N (curves). It is seen from the figures that the correspondence between the two nucleation treatments is reasonably good; thus the bulk nucleation behaviours will be similar in the two models. Differences will occur, however, on an element-by-element basis due to the random placement of particles mapped onto the FE mesh. Better matching of the nucleation treatment is possible, but requires tighter two-way coupling of the models and was considered beyond the scope of the current work.

Table 6.3 summarizes the controlling parameters used in the GTN-based damage simulations, corresponding to the curves in Fig. 6.6. Note that the standard deviation of void-nucleation strain, s_N, was reduced to 15 %, for the 1.0 mm sheets to reflect the effect of the rolling process. The thinner 1.0 mm sheet has a larger population of small particles compared to the 1.6 mm sheet. Note also that the value of f_N selected for each sheet was the higher of the measured particle areal fractions in the rolling- and transverse-through-thickness planes to facilitate a conservative prediction of flange formability. An initial porosity of zero ($f_0 = 0$) was chosen for both alloys based on metallographic analyses by Pilkey (private communication, 2001).

6.3.2 *Void Growth*

Void growth in the coupled model is treated using the predicted evolution of porosity within the GTN-based FE calculations. Within the percolation code, voids are assumed to enlarge during the deformation process according to

$$a^{(i)} = a^{(i-1)} \left(\frac{1 + f^{(i)}}{1 + f^{(i-1)}} \right)^{1/3} \tag{6.10}$$

where $a^{(i)}$ is the semi-axis of a void at the ith step and $f^{(i)}$ the porosity predicted for the corresponding parent finite element. This approach enforces equal rates of void growth between the GTN-based FE and percolation predictions.

Equation (6.10) implies that void expansion is isotropic and that details of local void geometry are neglected, such as the void aspect ratio and cluster effects addressed by Thomson et al. (1999). In addition, void growth under conditions of partial void-matrix separation hasn't been considered in the current study and the entire particle was treated as a void once nucleated.

Despite these simplifications, this void growth treatment is robust and can handle large changes in strain path using the isotropic Gurson void growth assumptions. Note that Eq. (5.10) naturally handles void closure effects that may occur during bend-unbend operations, for example.

6.3.3 Void Coalescence

Prediction of void coalescence is performed exclusively within the percolation damage code. Void coalescence using the so-called critical void volume fraction criterion (Eq. 6.3) within the GTN-based damage model is suppressed. Void coalescence was predicted using the modified version of Brown and Embury's (1973) ligament to void size ratio criterion, as described previously in Sect. 5.1.2.3.

In real forming operations, the strain field and strain path in the part are complex; hence, restrictions on ligament orientation for coalescence expressed by Eq. (5.6) were eliminated in the coupled model. The search algorithm used to predict void coalescence utilizes the nearest neighbour list generated by the tessellation software. At each strain increment step, Eqs. (5.2), (5.3), (5.4), (5.5) and (6.9), (6.10) are applied to all neighbouring pairs of nucleated voids. Note that the neighbouring particle search list spans across neighbouring elements in the finite element mesh.

6.3.4 Post-coalescence Treatment

The void-crack and crack-crack coalescence treatments are the same as described in Sect. 5.1 for the uniform strain model. In the coupled model, however, cracks are assigned to a parent element based on the location of their centroids. At each step, crack growth is predicted based upon the hydrostatic plastic strain component of its parent element with

$$a_m^{(i)} = a_m^{(i-1)} \left(\frac{1 + \varepsilon_{kk}^{(i)}}{1 + \varepsilon_{kk}^{(i-1)}} \right)^{1/3} \tag{6.11}$$

where $a_m^{(i)}$ is the semi-axis of a crack and $\varepsilon_{kk}^{(i)}$ is the hydrostatic strain at the ith step.

6.4 Particle Field Mapping

In coupled model, one of the most significant changes in damage percolation code is the mapping of the particle field onto the FE mesh AOI. Figure 6.7 shows a typical mesh AOI and mapped second phase particle field for 1.6 mm AA5182. This mapping requires the assignment of a parent element to each second phase particle.

A straightforward search algorithm is used to assign each particle a parent element. Damage evolution within the particle sub-field of each element is governed by the stress, strain and porosity history of the parent. For each time step, particle, void and crack positions are updated through linear interpolation of the nodal displacements of their parent elements, which can be expressed as

$$x_k = \sum_{j=1}^{4} N_j(s,t) X_k^j \tag{6.12}$$

where: N_j are the standard shape functions for a linear iso-parametric finite element; $j = 1, 2, 3, 4$ refers to nodal label; x_k and X_k^j are the respective coordinates of the centroid of a crack or particle and the nodes of its parent element; and s and t are the local coordinates of the crack or particle centroid within its parent element.

Cracks formed by coalescence of voids and/or cracks are also assigned to parent elements once coalescence occurs. A search algorithm is used to assign a parent element to each crack. Once a new crack is formed, the coordinates of its centroid can change and shift from one element to another due to coalescence of additional voids or cracks situated amongst different elements.

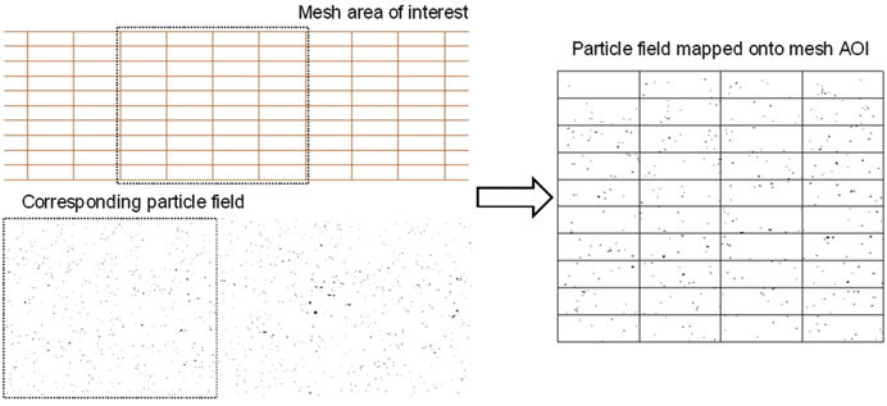

Fig. 6.7 A particle field is mapped onto the mesh area of interest from a larger tessellated second phase particle field of AA5182 sheet (Reprinted with permission from Chen et al. (2005). Copyright: Elsevier)

6.5 Coupled Model – Mesh and Particle Fields

6.5.1 FE Mesh

To save computation cost, axisymmetric solid continuum elements were employed in the FE part of the coupled model to model the blank and the rigid tooling because of the axisymmetric nature of the load and geometry. Calculations were performed using a commercial explicit dynamic FE code, LS-DYNA (Hallquist 2006). This code was linked with a user-supplied constitutive model embodying the Gurson constitutive model, developed by Worswick and Pelletier (1998).

The mesh adopted for the tooling and blank is shown in Fig. 6.8. Four-node, linear quadratic elements were used, with ten and six elements through the thickness of 1.6 mm and 1.0 mm blanks, respectively. From the predicted contours of porosity in the blank, it was found that maximum porosity always occurred in the area initially located right above the top of the male drawbead. Therefore, a finer mesh is employed in that area and this region was adopted as the mesh AOI for the subsequent damage percolation simulation. To further examine the bending/unbending effect on damage development during stretch flange forming, the top and bottom elements, designated elements A and B, were used to track damage histories.

The tooling elements were modelled as rigid and penalty function-based contact interfaces were defined between the tooling surfaces and the blank (Hallquist 2006).

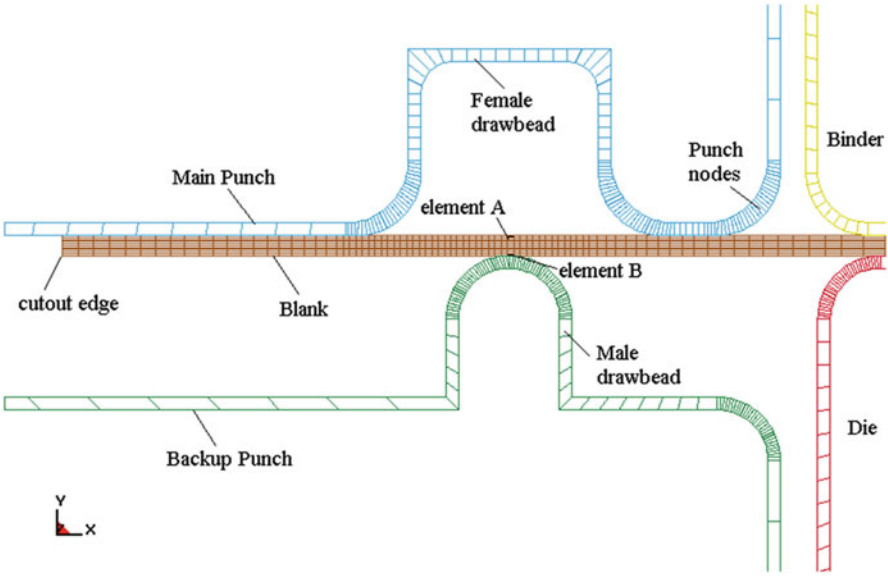

Fig. 6.8 Axisymmetric FE mesh used to model the stretch flange forming, 1.6 mm gauge, 92 mm cutout is shown (Reprinted with permission from Chen et al. (2005). Copyright: Elsevier)

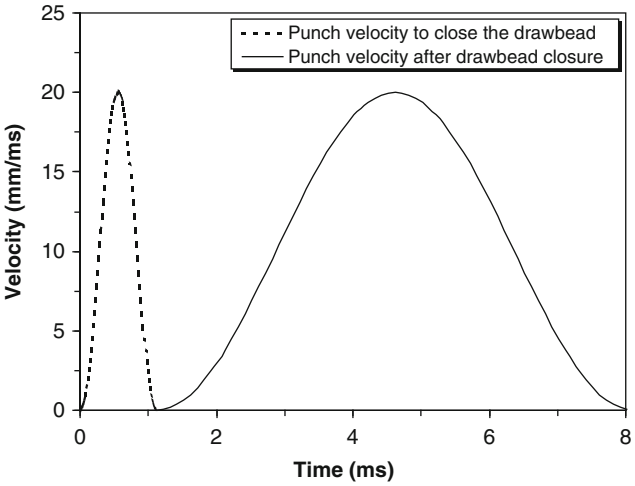

Fig. 6.9 Velocity histories of the main punch and backup punch in stretch flange forming (Reprinted with permission from Chen et al. (2005). Copyright: Elsevier)

A coefficient of friction of 0.074 (Draw-sol) was selected at all the interfaces between the blank and the punches for AA5182 based upon the drawbead simulator test data (Chen 2004). The blank interfaces with the die and binder were assigned a friction coefficient of 0.15 (dry friction) in order to minimize draw-in.

6.5.2 Boundary Conditions – Tooling Motion

A clamping force of 378 kN is applied on the binder to hold the blank during the forming operation. Before the bead is closed, a prescribed sinusoidal velocity (Fig. 6.9) is used to move the backup punch upwards to close the bead. After the drawbead is closed, the kinematic constraint on the backup punch is removed and replaced with a clamping force of 222.5 kN that holds the bead closed during the main punch motion. Once the backup punch force is applied, the main punch moves downward, expanding the stretch flange cutout. The velocity history prescribed for the main and backup punches are displayed in Fig. 6.9. A sinusoidal velocity profile is adopted to control or limit inertial effects. The forming operation is terminated once the main punch reaches its limit position.

6.5.3 Second Phase Particle Fields

1.0 and 1.6 mm AA5182 sheets were considered in stretch-flange forming simulations. The second-phase particle field information described in Chap. 5 was adopted in the simulation. Table 6.4 lists relevant data from the measured particle fields used in the simulations.

Table 6.4 Particle field used in the coupled FE/damage percolation modelling

Material	AA5182_1.0	AA5182_1.6
Particle areal fraction (%)	0.768	0.8531
Number of particles	8,486	13,038
Particle field size (mm)	4.4 × 1.0	4.4 × 1.6

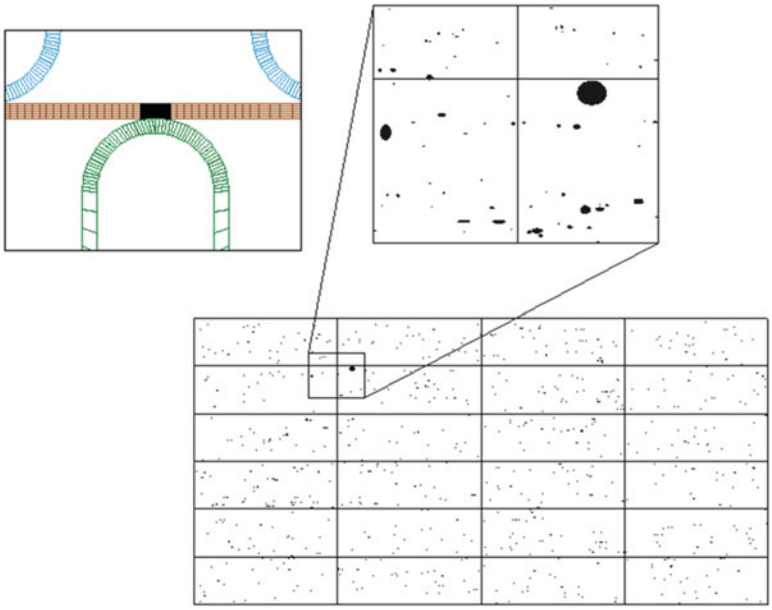

Fig. 6.10 Initial position of the mesh AOI and the corresponding mapped particle field, 1.0 mm AA5182

In the damage percolation simulations of stretch flange forming, particle fields of roughly 14,300 × 7,000 pixels (2.0 × 1.0 mm) and 14,300 × 11,400 pixels (2.0 × 1.6 mm) were separated from the original large particle fields and mapped onto a mesh area of either 24 elements (4 × 6) or 40 elements (4 × 10), respectively, located immediately above the male drawbead. This region was the most severely damaged area in the coalescence-suppressed GTN-based FE simulation. Damage percolation simulations were performed for this area using the coupled approach. Figs. 6.10 and 6.11 show the mesh areas of interest and the corresponding mapped particle fields used for 1.0 mm and 1.6 mm AA5182.

6.6 GTN-Based FE Results

In developing a coupled simulation of a forming operation it is first necessary to identify the worst-damaged area in the part; this becomes the damage AOI for the percolation simulation. In order to locate this region, several considerations are

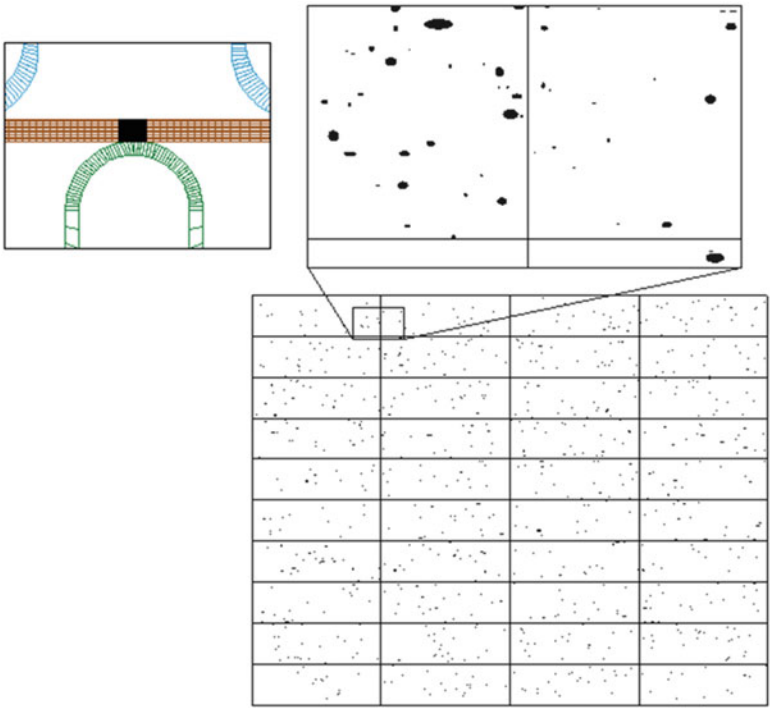

Fig. 6.11 Initial position of the mesh AOI and the corresponding mapped particle field, 1.6 mm AA5182 (Reprinted with permission from Chen et al. (2005). Copyright: Elsevier)

important. First, the GTN-based FE simulation is conducted to ascertain the potential most-damaged areas. Then damage percolation simulations are performed using the element and nodal data for each region. It is important to consider several candidate regions since the region of highest damage may differ between the GTN-based and percolation damage-based calculations. Finally, the region to fail at the lowest punch depth is taken as the most damaged area for the coupled model.

Such a procedure was used to determine the most damaged area for the coupled model. For all the blanks and materials considered in this study, it was found that the area initially located immediately above the top of the drawbead was the most damaged region. Therefore, this region was adopted as the mesh AOI for all of the models presented here.

6.6.1 Porosity Predictions

The predicted porosity levels are strongly related to sheet thickness. Figures 6.12 and 6.13 show a sequence of deformed contour plots of porosity for the 1.0 and 1.6 mm AA5182 samples with an 88 mm radius cutout, using a nucleation strain of

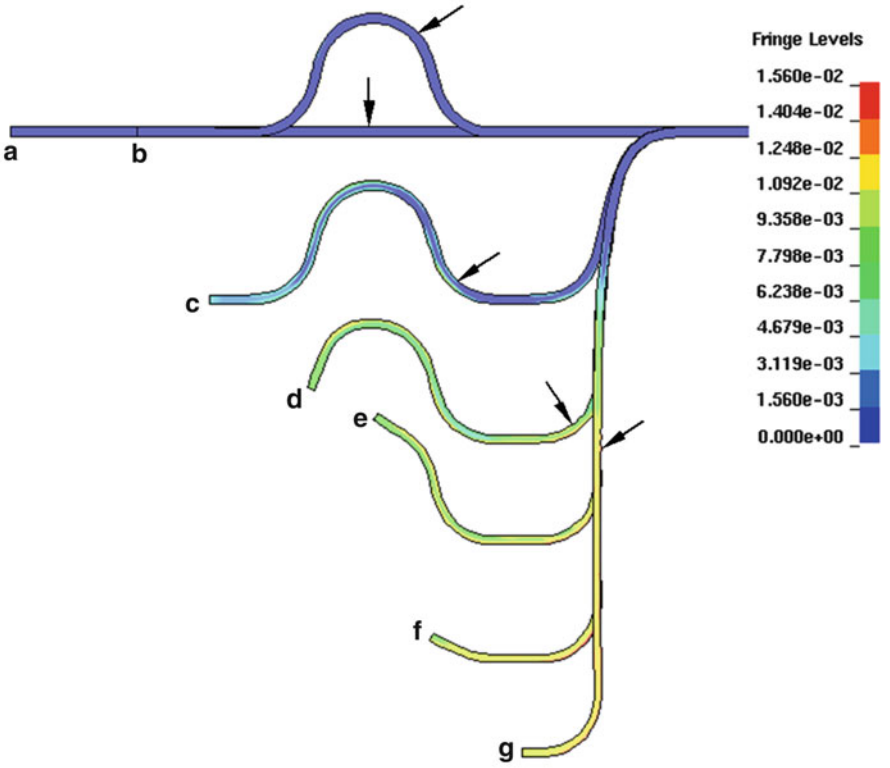

Fig. 6.12 Porosity contours within a deformed AA5182, 1.0 mm stretch flange with an 88 mm cutout using void nucleation strain, $\varepsilon_N = 0.2$ (coalescence-suppressed GTN-based FE calculation): (**a**) initial position; (**b**) drawbead closure at $t = 1.125$ ms; (c) $t = 3.6$ ms (punch depth = 16.4 mm); (**d**) $t = 4.4$ ms (punch depth = 30.1 mm); (**e**) $t = 4.88$ ms (punch depth = 40.1 mm); (**f**) $t = 5.5$ ms (punch depth = 51.7 mm); (**g**) $t = 6.1$ ms (punch depth = 60.9 mm). The arrows serve to locate the AOI

0.2. Much lower levels of void nucleation occur during drawbead closure for the 1.0 mm sheet due to the lower bending strain within the drawbead. With punch movement, the maximum porosity increases to 1.6 % for the 1.0 mm sheet compared to 2.1 % for the 1.6 mm sheet.

The progression of damage development for a higher nucleation strain is shown in Fig. 6.14. These are the sequences of porosity contours for the 1.6 mm AA5182 sample with an 88 mm radius cutout, considering nucleation strain of 0.6. Comparison of this figure to Fig. 6.13 demonstrates that the level of the void nucleation strain greatly affects the predicted level of damage in the samples. Higher void nucleation strain levels retard void initiation and result in lower porosity levels. As the void nucleation strain increases from 0.2 to 0.6, the maximum porosity in the deformed part decreases from 2.1 to 1.4 %, as indicated in the figures. In addition, the void nucleation strain has strong impact on damage development during

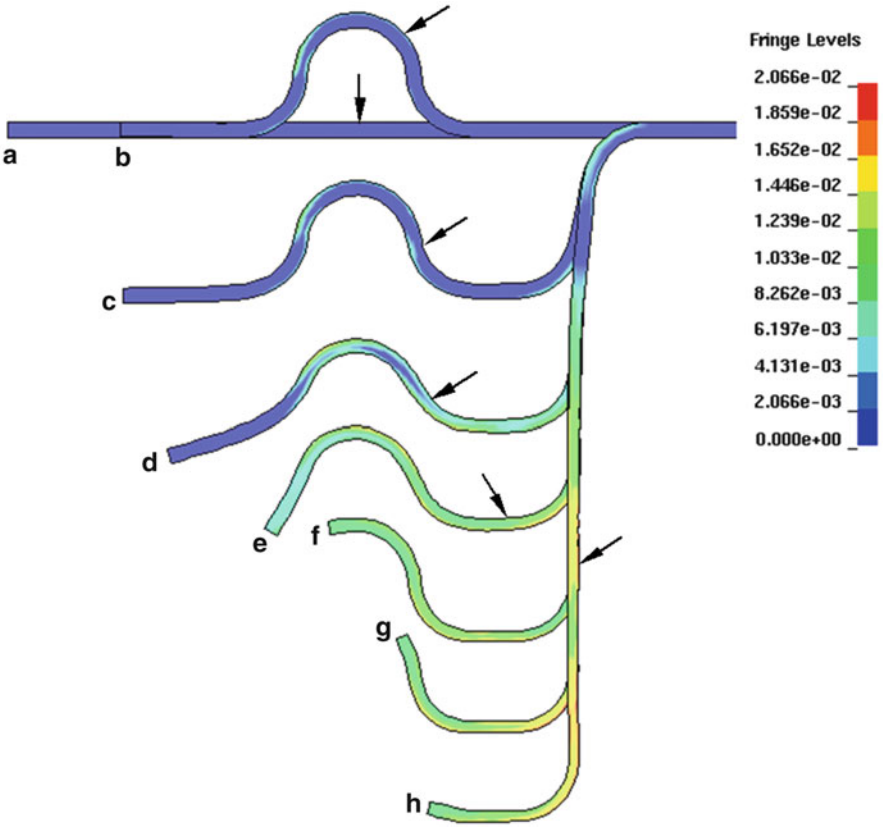

Fig. 6.13 Porosity contours within a deformed AA5182, 1.6 mm stretch flange with an 88 mm cutout using void nucleation strain, $\varepsilon_N = 0.2$ (coalescence-suppressed GTN-based FE calculation): (**a**) initial position; (**b**) drawbead closure at $t = 1.125$ ms; (**c**) $t = 3.6$ ms (punch depth = 16.4 mm); (**d**) $t = 4.4$ ms (punch depth = 30.1 mm); (**e**) $t = 4.88$ ms (punch depth = 40.1 mm); (**f**) $t = 5.5$ ms (punch depth = 51.7 mm); (**g**) $t = 6.1$ ms (punch depth = 60.9 mm); (**h**) $t = 8.1$ ms (punch depth = 70 mm). The arrows serve to locate the AOI (Reprinted with permission from Chen et al. (2005). Copyright: Elsevier)

drawbead closure (Figs. 6.13b and 6.14b). For a nucleation strain of 0.2, significant void nucleation is predicted during drawbead closure. However, for a nucleation strain of 0.6, the predicted void nucleation during drawbead closure was very low. For 1.0 mm sheet, damage development within the stretch flanges exhibits similar dependence on nucleation strain (not shown).

Figure 6.15 summarizes graphically the predicted peak porosity values for all of the stretch flange cases modelled. For both thicknesses, the peak porosity is strongly dependent on the nucleation strain level. Higher nucleation strain leads to lower peak porosity. The peak porosity in the 1.6 mm sheet does not show a dependence on cutout size, within the range considered. On the other hand, the peak porosity of the 1.0 mm sheet does indicate a mild, cutout-size dependence at a nucleation strain level of 0.2; that is, larger cutouts induce lower peak porosities. The 1.0 mm sheet exhibits much lower peak porosity in comparison to the 1.6 mm sheet.

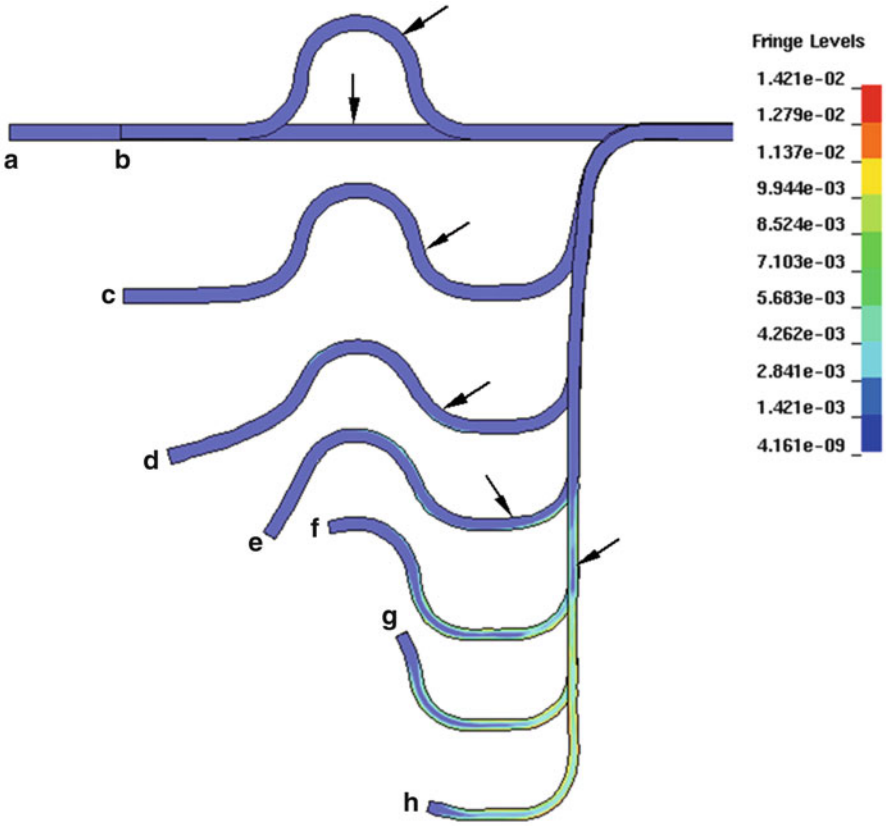

Fig. 6.14 Porosity contours within a deformed AA5182, 1.6 mm stretch flange with an 88 mm cutout using void nucleation strain, $\varepsilon_N = 0.6$ (coalescence-suppressed GTN-based FE calculation): (**a**) initial position; (**b**) drawbead closure at t =1.125 ms; (**c**) t = 3.6 ms (punch depth = 16.4 mm); (**d**) t = 4.4 ms (punch depth = 30.1 mm); (**e**) t = 4.88 ms (punch depth = 40.1 mm); (**f**) t = 5.5 ms (punch depth = 51.7 mm); (**g**) t = 6.1 ms (punch depth = 60.9 mm); (**h**) t = 8.1 ms (punch depth = 70 mm). The arrows serve to locate the AOI

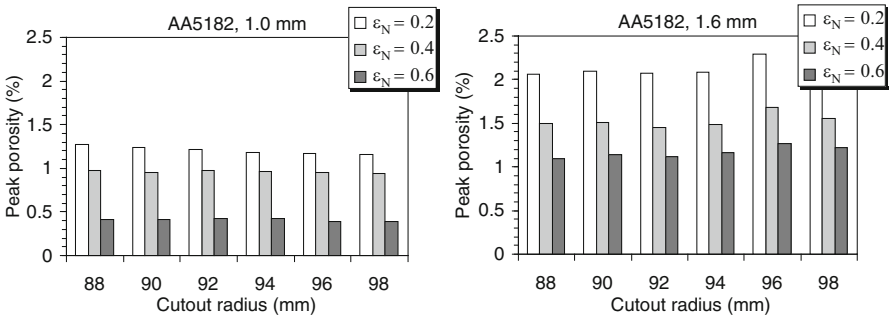

Fig. 6.15 Peak porosity as a function of flange cutout radius

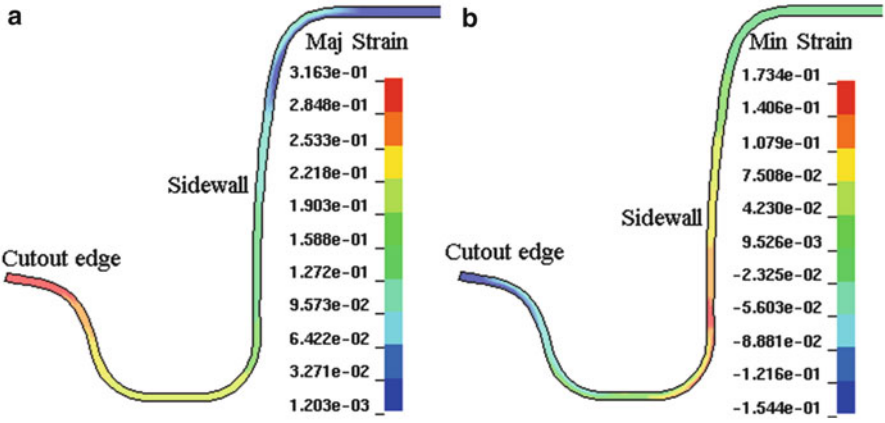

Fig. 6.16 Fringe plot of predicted major (**a**) and minor (**b**) strain for 1.0 mm AA5182 with 88 mm radius cutout at punch depth of 37.8 mm

6.6.2 Strain Analysis

Figure 6.16 shows fringe plots of predicted in-plane major and minor strains for the 1.0 mm sample with an 88 mm cutout. The punch depth corresponds to 90 % of the limit punch depth to fracture determined by the experiment (Chen 2004). It is evident that for the 1.0 mm AA5182 sheet, the cutout edge exhibits the maximum major strain. The same data was obtained for the 1.6 mm samples (although not shown), which shows that the largest major strain occurs at the punch nose in the sidewall region. This transition is due to the higher drawbead restraint for the thicker sheet.

The minor strain plots in both figures serve to illustrate the nature of the strain state in the stretch flanges. The minor strains are negative at the cutout indicating a draw state whereas the minor strains are tensile in the sidewall, corresponding to a stretch condition.

The strain distributions predicted by the FE calculation were compared to the measured results (Chen 2004), to assess the current FE approach. The true strain distributions are plotted as loci of in-plane major versus minor strain for a line of circular grids or elements, running radially from the cutout periphery. Note that true (logarithmic) strains were plotted for the 90 % punch depth cases. Figure 6.17 shows the predicted and measured strain distributions for the 1.0 mm AA5182 sheet with an 88 mm cutout. It was found that void nucleation strain (ε_N) plays only a mild role in the predicted strain distributions, therefore, only the results for a nucleation strain of 0.4 are presented. From the cutout edge to the sidewall, the material experiences a transition from uniaxial tension (draw state) to biaxial stretching. The peak major strain occurs at the cutout edge. It is observed that the predicted strains are in good agreement with the measured values. Note that the predicted strains in the drawbead region display an "S" profile on either side of

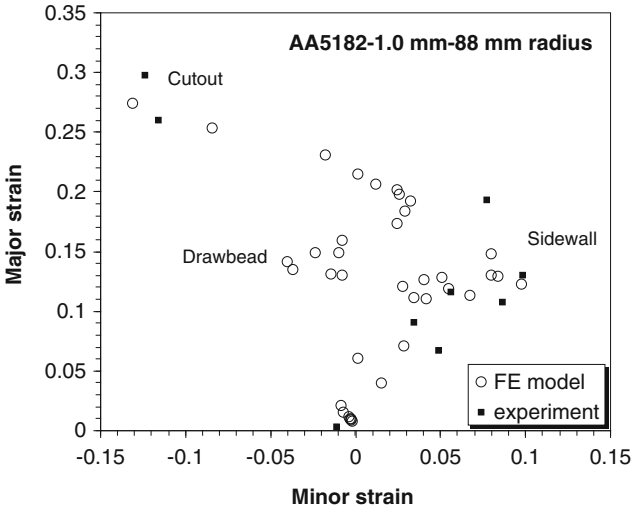

Fig. 6.17 Strain distribution for the 1.0 mm AA5182 with an 88 mm radius cutout

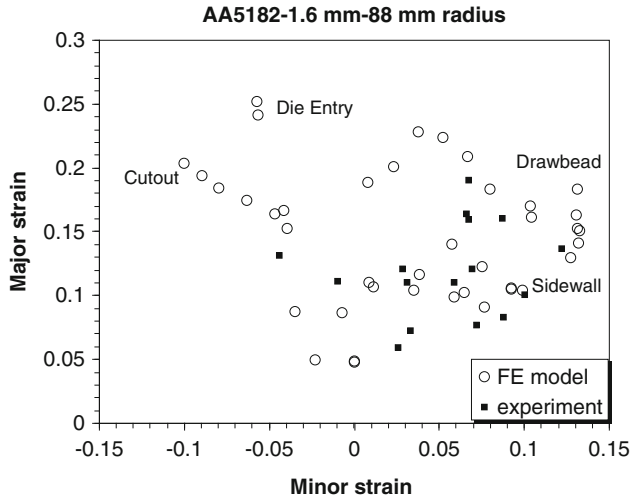

Fig. 6.18 Strain distribution for the 1.6 mm AA5182 with an 88 mm radius cutout

the plane strain axis ($\varepsilon_{\text{minor}} = 0$), representing the bending transitions. Recall that strain measurements were not possible in the drawbead region due to the sharp curvatures of the deformed sheet.

Figure 6.18 shows the strain distributions for the 1.6 mm samples, with an 88 mm radius cutout. In contrast to the 1.0 mm sheet, the material experiences much more complex deformation varying from the inner edge to the sidewall. The

much higher strains occur in the sidewall under biaxial stretching, due to the higher drawbead restraint. The strain predictions also compare well to the measured values for these thicker samples.

6.7 Coupled FE/Damage Percolation Predictions

The procedure described in Sect. 6.5 was applied to construct coupled FE/damage percolation models of the stretch flange experiments. This section presents the results from the percolation damage part of the simulations which are run as a post-processing operation based on the results predicted in the previous section. In particular, the effect of cutout size, sheet thickness and nucleation strain on formability is presented. The predicted formability is compared to the experimental results to assess the coupled FE/damage percolation model. Also presented are the results obtained for damage accumulation within the mapped particle fields. This data is compared with quantitative metallographic results from the interrupted samples.

6.7.1 Damage Evolution

Figure 6.19 shows a sequence of coupled-model predictions of damage development within the 1.6 mm stretch flange with a 98 mm radius cutout using $\varepsilon_N = 0.4$. Shown is the mapped particle field in a deformed state for six stages of the forming operation along with a close-up view of the FE mesh AOI and tooling in the corresponding deformed states. As in the results presented for the uniform strain fields in Chap. 5, particles are black and coalesced regions are indicated using gray ellipses. This sequence shows the general progression of the AOI as it slides around and along the tooling features. The predicted increase in damage is also evident as the number of coalesced regions increases with deformation.

Void nucleation initiates within the upper region of the particle field that undergoes bending. Primary void coalescence was observed within individual particle clusters during drawbead closure at $t = 1.1$ ms, as shown in Fig. 6.19b. Void coalescence developed within lower particle clusters when the material entered the second bend, but was still restricted to individual particle clusters, as shown in Fig. 6.19c. After exiting the second bend at $t = 4.5$ ms (Fig. 6.19d), a number of cracks (coalesced voids) were predicted within the lower region. Finally, as the material enters the third bend at the punch nose at $t = 4.9$ ms (Fig. 6.19e), the lower elements again experience tensile bending, causing void coalescence amongst more than four void clusters. After this event, any additional straining leads to catastrophic failure through macrocracking across the entire particle field without further straining (not shown).

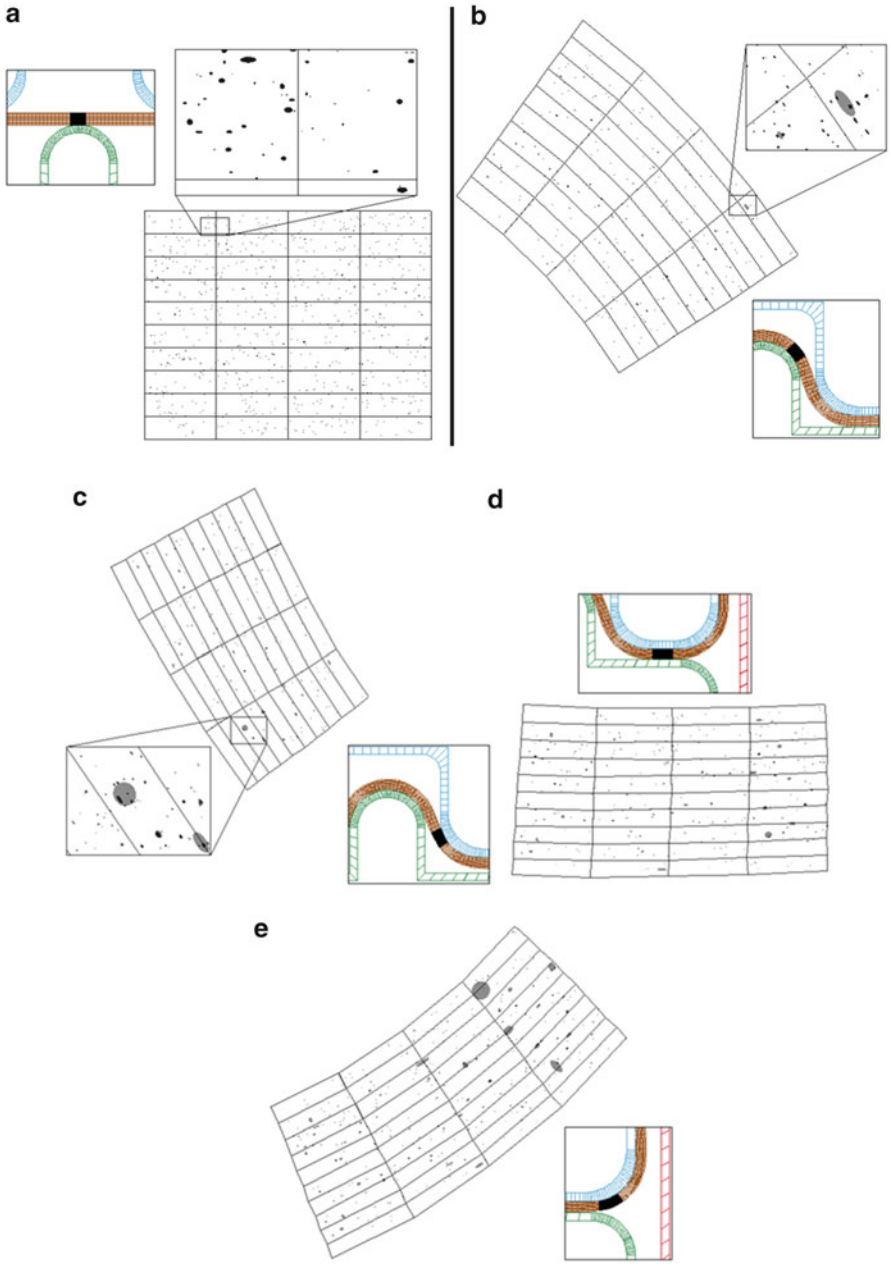

Fig. 6.19 A sequence of predicted damage development within the area of interest: AA5182 1.6 mm sheet with a 98 mm radius cutout at void nucleation strain of 0.40: (**a**) t = 0 ms (punch depth = 0); (**b**) t = 1.1 ms (punch depth = 0); (**c**) t = 4 ms (punch depth = 22.9 mm); (**d**) t = 4.5 ms (punch depth = 32.6 mm); (**e**) critical moment: t = 4.9 ms (punch depth = 40.1 mm) (Reprinted with permission from Chen et al. (2005). Copyright: Elsevier)

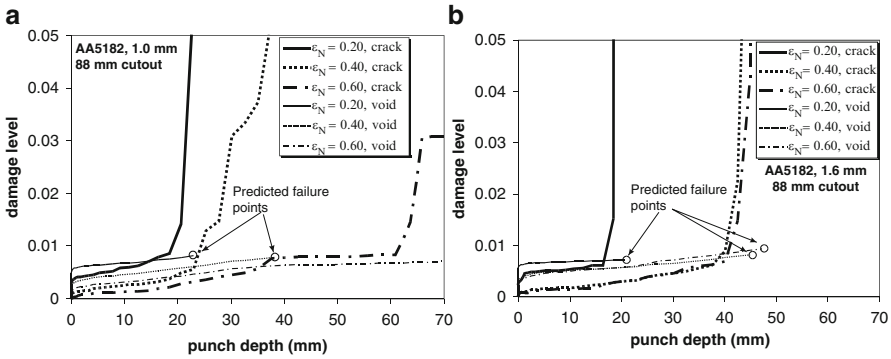

Fig. 6.20 Damage development against punch depth within the area of interest at different void nucleation strain levels, for 88 mm cutout, (**a**) 1.0 mm sheet; (**b**) 1.6 mm sheet

Damage development within the measured second phase particle fields of the 1.0 mm stretch flange displayed similar features (not shown). Generally, the onset of fracture is postponed compared to that for the 1.6 mm sheet, due to the lower restraint from the drawbead and the lower bending effect for the thinner 1.0 mm sheet.

6.7.2 Quantitative Damage Predictions

A more quantitative prediction of damage progression within the stretch flange samples can be obtained based upon predicted void and crack areal fractions averaged within the AOI. Figure 6.20 plots the predicted damage level versus punch depth for both thicknesses. Plotted are time histories of areal fraction as a function of punch depth for three levels of void nucleation strain. From these results, stretch flange formability can be predicted in terms of the limit punch depth; that is, the punch depth at which the crack areal fraction grows without further punch depth increment.

It is evident that higher nucleation strains in the percolation model will lead to a higher predicted formability, as seen in the figures. In addition, the predictions reveal a much lower damage rate for the thinner sheet materials.

The prediction for the thicker gauge material suggests much higher damage levels (Fig. 6.20b). This is consistent with fracture occurring at the punch nose due to the higher drawbead restraint and bending strains within the drawbead.

The effect of cutout size on the onset of profuse void coalescence can be seen in Fig. 6.21. Plotted is the predicted crack areal fraction for the range of cutout radii considered for the 1.6 mm AA5182 samples. The effect of cutout size on damage development is much smaller than nucleation strain, at least for the range of cutout sizes considered.

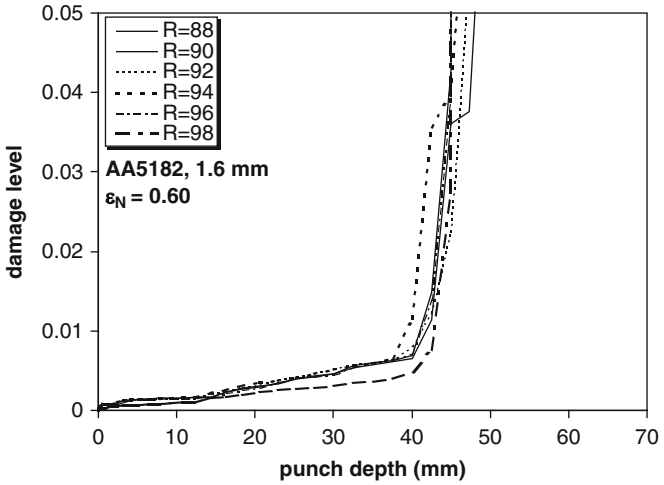

Fig. 6.21 Damage development against punch depth for various cutout radius of 1.6 mm AA5182 sheet, $\varepsilon_N = 0.60$ (Reprinted with permission from Chen et al. (2005). Copyright: Elsevier)

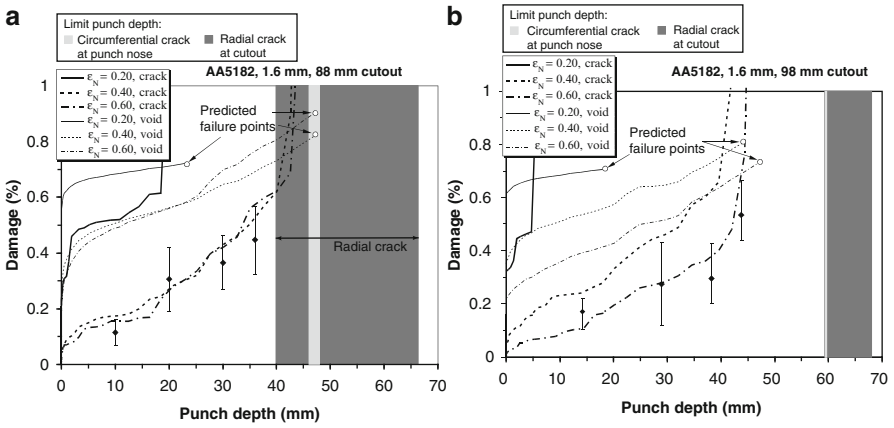

Fig. 6.22 Damage development within the area of interest obtained from quantitative metallography compared to the coupled FE/damage percolation modeling for 1.6 mm flange with (**a**) 88 mm cutout; (**b**) 98 mm cutout (Reprinted with permission from Chen et al. (2005). Copyright: Elsevier)

6.7.3 Comparison with Measured Damage Levels

Damage development within the area of interest was obtained from quantitative metallography and is plotted for comparison with the predicted results in Figs. 6.22 and 6.23. The average porosity level is plotted (symbols) along with a scatter bar corresponding to the standard deviation in porosity for the acquired images.

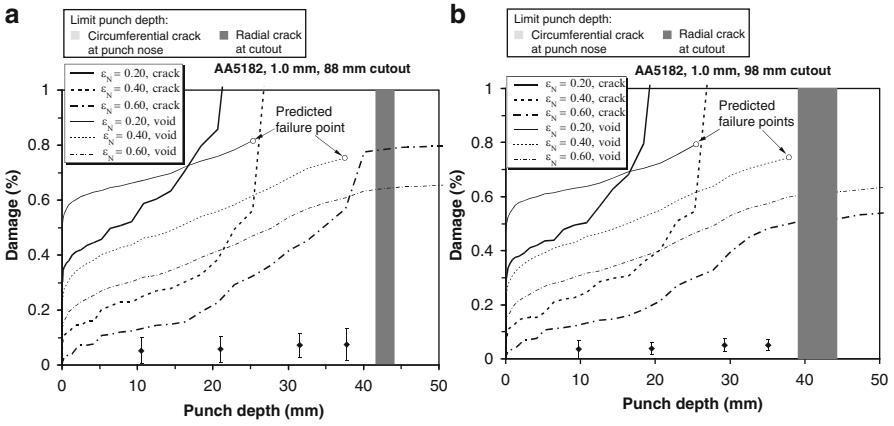

Fig. 6.23 Damage development within the area of interest obtained from quantitative metallography compared to the coupled FE/damage percolation modeling for 1.0 mm flange with (**a**) 88 mm cutout; (**b**) 98 mm cutout

The shaded regions indicate the upper and lower limit in measured punch depths to fracture from the stretch flange tests (Chen 2004). Note that the figures show both the predicted areal fractions of cracks and voids. As defined in the preceding chapter, in the damage percolation model, the "cracks" correspond to the large elliptical void bounding all voids comprising the crack and leads to an overestimate of damage. Thus the predicted void areal fraction should be compared to the measured data. From examination of Fig. 6.22, it is seen that the predicted damage development generally lies above the measured data from the 1.6 mm sheet.

The predicted damage development for the 1.0 mm stretch flange is also larger than the measured data, as seen in Fig. 6.23. The reason for this consistent over-prediction is uncertain. One reason for this apparent over-prediction in porosity lies in the nucleation model which assumes the entire particle to become void upon nucleation. Nonetheless, the predicted damage rate for the 1.0 mm samples is much lower than that for the 1.6 mm samples, as seen by comparing Figs. 6.23 and 6.22 for example. This ranking of the effect of the sheet thickness is at least in qualitative accord with the measured damage levels.

6.7.4 Formability Predictions

In this section, the formability predictions for the four alloy-thickness combinations are presented as a function of cutout radius and nucleation strain.

Figure 6.24 shows the predicted limit punch depth to fracture versus cutout radius. The predicted punch depths are plotted for each of the void nucleation strain levels considered. Also plotted are the measured limit punch depths from the experiments.

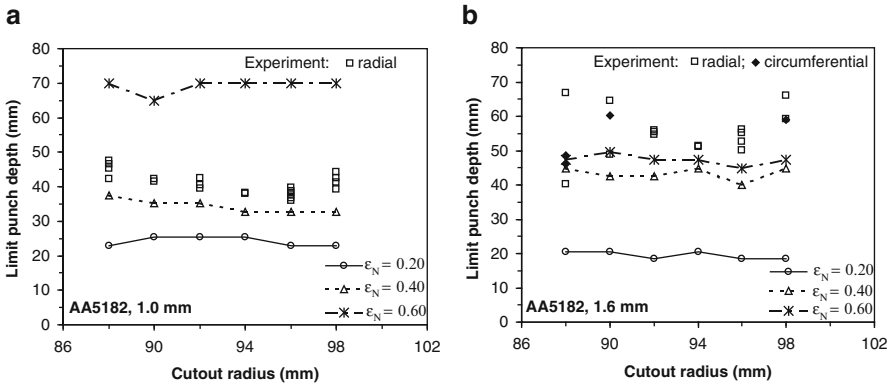

Fig. 6.24 Limit punch depth to fracture versus cutout radius predicted by the coupled FE/damage percolation modeling, (**a**) 1.0 mm sheet, (**b**) 1.6 mm sheet (Figure (**b**) was reprinted with permission from Chen et. al. (2005). Copyright: Elsevier)

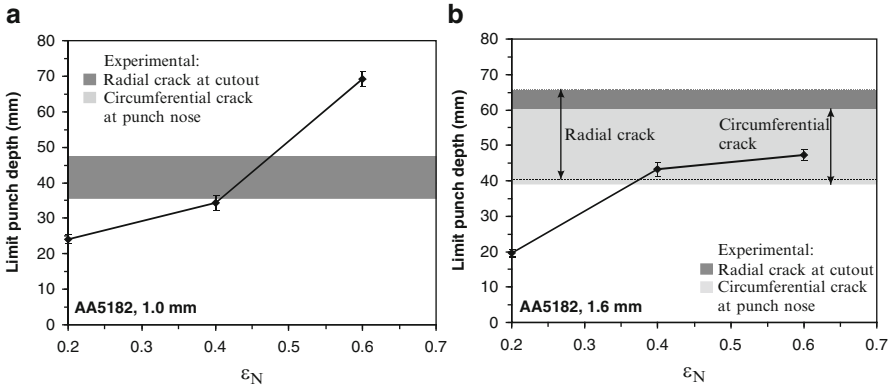

Fig. 6.25 Limit punch depth versus void nucleation strain, (**a**) 1.0 mm sheet; (**b**) 1.6 mm sheet

For the 1.6 mm sheet, at a nucleation strain of 0.4, the predicted limit punch depth to fracture varies between 40 and 45 mm as cutout radius increases from 88 mm to 98 mm. The predicted limit punch depth increases slightly from below 45 mm to about 45–50 mm as void nucleation strain increases from 0.4 to 0.6. However, the average limit punch depth to fracture predicted drops to about 20 mm as the nucleation strain is lowered to 0.2.

It is evident from this figure that the effect of cutout radius on formability is relatively weak, at least for the range of cutout radius considered. The effect of void nucleation strain is very large; this is further examined in Fig. 6.25 which plots limit punch depth as a function of nucleation strain. The curves in each figure correspond to the numerical predictions. The scatter bands correspond to the variation in predicted punch depth with cutout size. The shaded regions indicate the upper and lower limit in measured punch depth from the experiments. The darker region

indicates the radial failures at the cutout edge and the lighter shading corresponds to circumferential failures at the punch profile radius. Note that the maximum punch depth considered was 70 mm; thus, the predictions plotted at this level have not failed. Several observations can be made:

- The dependency of predicted punch depth on nucleation strain is very strong and overwhelms any effect due to cutout radius for the range considered;
- The scatter in the experiments is very large and of similar magnitude to the range of the limit punch depth in the models.

In spite of the experimental scatter, there exists a qualitative agreement between the predicted and measured limit punch depths. The results indicate that a nucleation strain in the range 0.25–0.5 would lead to predicted limit punch depths in general accord with the observed failures for the model AA5182. These values are consistent with current results by Winkler (2003).

Further refinement of the material damage parameters is not thought possible at this time, pending improved repeatability of the stretch flange experiments and/or more in-depth metallographic studies of nucleation behaviour for these alloys (Winkler 2003).

6.8 Summary

Stretch flange formability, in terms of limit punch depth to fracture, is predicted through the coupled model as a function of cutout radius and void nucleation strain. The experiments and models have shown that the limit punch depth to fracture is not particularly sensitive to the variation of cutout size within the range considered. The predicted damage rate, however, did decrease with an increase in cutout size. Increased sheet thickness leads to an increase in damage rate in the models, favouring circumferential cracking at the punch nose. This trend was reflected in higher predicted damage rates and a transition to punch nose failures for the thicker AA5182 samples.

The void nucleation strain has a strong impact on the predicted damage rate and formability. Higher nucleation strain leads to higher predicted formability and lower damage rate. Comparison of the predicted formability and damage rate with experimental results suggests a nucleation strain of 0.2–0.5 for these alloys.